Coupling Scattering Characteristic Analysis of Dihedral Corner Reflectors in SAR Images

ZHIMING XU[iD], **XIAOFENG AI, QIHUA WU**[iD], **FENG ZHAO, AND SHUNPING XIAO**

State Key Laboratory of Complex Electromagnetic Environmental Effects on Electronics and Information System, National University of Defense Technology, Changsha 410073, China

Corresponding author: Xiaofeng Ai (anxifu2001@163.com)

ABSTRACT The scattering mechanisms of dihedral corner reflectors have attracted great attention in the past decades. However, the scattering centers of dihedral corners are not discussed systematically. In this paper, the multi-bouncing scattering mechanism of dihedral corners is analyzed in detail based on the scattering characteristics of polygon plates and ray-tracing technique. Furthermore, the coupling scattering center (CSC) is proposed as a detailed explanation of the multi-bouncing scattering mechanism of dihedral corners and the locations of CSCs in the high-resolution range profile are deduced based on the monostatic-and-bistatic equivalence theorem. CSCs give a precise description of target structures and can improve the ability of radar target recognition. Finally, the simulation results via electromagnetic computation validate the theoretical analysis.

INDEX TERMS Dihedral corner reflector, coupling scattering center (CSC), auto target recognition (ATR), synthetic aperture radar (SAR).

I. INTRODUCTION

Synthetic Aperture Radar (SAR) has attracted the great interest due to its ability to work day and night under adverse weather condition [1]–[3]. It is widely applied in Automatic Target Recognition (ATR) [4]–[7]. ATR can be classified into two categories: template-based method and model-based method [8]. Due to the simpler realization, the template-based algorithm is first applied. However, the template-based algorithm requires huge memory and is difficult to recognize targets in real time. The model-based algorithm has attracted great attention thanks to overcoming these drawbacks by establishing the physical or mathematical model of targets, such as parametric scattering center models [9], [10]. Most model-based algorithms utilize the attributed scattering center (ASC) model to extract target features currently [11], [12]. However, ASC model could not describe some types of scattering centers accurately such as the scattering center induced by creeping waves and traveling wave in the bistatic radar mode [13], the scattering center sliding on the target curved-surface and edges [14] and the scattering center induced by multi-bouncing scattering. It may lead to the mistakes in feature extraction. Therefore, these types of scattering centers should be further investigated to improve the performance of ATR. Furthermore, there are only

a few literatures investigating the characteristics of scattering centers induced by multi-bouncing scattering, to the best of our knowledge. The multi-bounce scattering widely exists in SAR echoes and involves key information of target structure. Consequently, investigating the characteristics of scattering centers induced by the multi-bounce scattering is of significance for SAR ATR.

Dihedral corners have attracted great attention due to abroad application. Firstly, the application of dihedral corners for the calibration of monostatic and bistatic polarimetric radar systems has been investigated in [15]–[18]. Secondly, dihedral corners are basic structures of complex objects and abstract models of tree trunk-ground interface [19], building walls [20] and building-road interactions [21]. Consequently, scattering characteristics of dihedral corners are critical to ATR. References [21]–[24] have investigated the scattering computation for monostatic radar and bistatic radar. However, the scattering centers of dihedral corners are seldom discussed.

Due to the high resolution of SAR, it is not conducive to the target recognition if the dihedral corners continue to be regarded as the point targets. According to the aspect dependences of scattering amplitude and position of scattering centers, the scattering centers are classified into

three types [25]: localized scattering center (LSC), distributed scattering center (DSC), and sliding scattering center (SSC). Without regard to the coupling between two plates, the single-bouncing scattering characteristics of dihedral corners can be analyzed by investigating two plates scattering respectively. The scattering characteristics of polygon plates are presented in section II. Different from the single-bouncing scattering, the multi-bouncing scattering considers the interaction between target components. The multi-bouncing scattering characteristics cannot be described by the listed scattering centers accurately. Therefore, the coupling scattering center (CSC) is proposed to analyze the multi-bouncing scattering characteristics in this paper. The CSC corresponds to the mechanism of multiple reflections and can be applied to analyze the coupling structures such as dihedral corners and cavity. Conventional SAR usually considers direct reflection echoes from targets. Therefore, ghosting artifacts and resolution reduction in SAR images will emerge when the multi-bounce echoes are superposed in the direct reflection echoes [26]. Some algorithms are employed to mitigate the influence of multipath in SAR images [27]–[29]. However, these ghosting artifacts can be regarded as CSCs and provide more information on the target structure.

The remainder of this paper is organized as follows: Section II deduces the position and amplitude of scattering centers of polygon plates, which is the basis of analyzing the multi-bouncing scattering mechanism of dihedral corners. Section III focuses on CSCs. This section gives a detailed explanation of multi-bouncing scattering mechanism of dihedral corners. The positions of CSCs in the high-resolution range profile (HRRP) are deduced. Section IV conducts SAR imaging simulations and analyzes the scattering characteristics of dihedral corners based on SAR images. Finally, conclusions are drawn in Section V.

II. SCATTERING CHARACTERISTICS OF POLYGON PLATE IN SAR IMAGES
A. SCATTERING CHARACTERISTICS OF POLYGON PLATE
Since conventional dihedral corners are composed of two polygon plates, the single-bouncing scattering characteristics of dihedral corners can be obtained by analyzing the scattering characteristics of polygon plates. In this section, it is revealed that the scattering characteristics of all polygon plates are consistent and the scattering centers originate in discontinuous place, i.e. edges or vertices.

As shown in Fig. 1, the scattering field formula of the polygon can be derived from the Stratton-Chu integral equation.

$$\mathbf{E_s}\left(\mathbf{r}\right) \cong 2 \iint \left\{ jw\mu \left[\hat{\mathbf{n}} \times \mathbf{H_i}\left(\mathbf{r}'\right)\right] G + \left[\hat{\mathbf{n}} \cdot \mathbf{E_i}\left(\mathbf{r}'\right)\right] \nabla' G \right\} dS'$$

$$\mathbf{H_s}\left(\mathbf{r}\right) \cong 2 \iint \left\{ \left[\hat{\mathbf{n}} \times \mathbf{H_i}\left(\mathbf{r}'\right)\right] \times \nabla' G \right\} dS' \quad (1)$$

where w is the angular frequency of the incident wave, μ is the magnetic permeability, G is the Green function, $\hat{\mathbf{r}}$ is a unit vector of reflective wave direction, $\mathbf{r}'$ is a vector lying in the

polygon plates, $\hat{\mathbf{n}}$ is the unit normal to polygon plate, pointing into the half-space containing the point P, ∇' denotes the derivation at $\mathbf{r}'$, and $\mathbf{r}$ is the position vector of the observation point P.

Since the electric and magnetic fields are mutually determined, only $\mathbf{E_s}\left(\mathbf{r}\right)$ is taken into consideration here.

The incident magnetic field is

$$\mathbf{H_i}(\mathbf{r}') = \boldsymbol{\varphi} H_0 \quad (2)$$

where H_0 is the intensity of the incident magnetic field and $\boldsymbol{\varphi}$ is the unit vector of the spherical coordinate system.

$\mathbf{E_s}\left(\mathbf{r}\right)$ is determined by $\mathbf{H_i}(\mathbf{r}')$, then

$$\mathbf{E_s}(\mathbf{r}) = -2j\eta k \frac{\exp(jk \|\mathbf{r}\|_2)}{4\pi \|\mathbf{r}\|_2} \cdot \iint \hat{\mathbf{r}} \times \left[\hat{\mathbf{r}} \times \left(\hat{\mathbf{n}} \times \mathbf{H_i}\left(\mathbf{r}'\right)\right)\right]$$
$$\times \exp\left[-jk\left(\hat{\mathbf{r}} - \hat{\mathbf{i}}\right) \cdot \mathbf{r}'\right] dS' \quad (3)$$

where $\hat{\mathbf{i}}$ in the unit vector of incident wave direction, η is the wave impedance and $k = 2\pi/\lambda$.
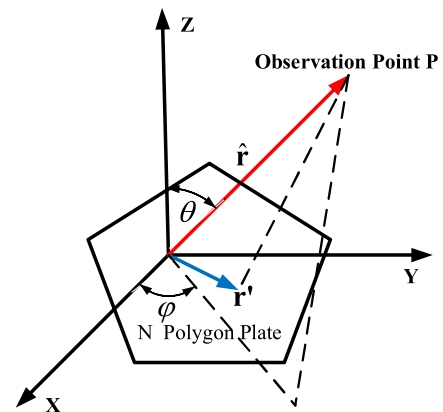

FIGURE 1. The scattering geometry of a polygon plate.

The polygon plate lies along the *x-y* plane as shown in Fig. 1 and the electric field of the polygon plate can be simplified as follows in the case of monostatic radar.

$$\mathbf{E_s}(\mathbf{r}) \cong -2j\eta k \frac{\exp(jk\|\mathbf{r}\|_2)}{4\pi\|\mathbf{r}\|_2} \boldsymbol{\theta} \cos\theta H_0 \iint \exp(-2j\mathbf{k_s} \cdot \mathbf{r}')dS' \quad (4)$$

where $\boldsymbol{\theta}$ is the unit vector of the spherical coordinate system and $\mathbf{k_s} = k\hat{\mathbf{r}}$

Eq.(4) can be rewritten as

$$\mathbf{E_s}\left(\mathbf{r}\right) \cong -2j\eta k \frac{\exp(jk\|\mathbf{r}\|_2)}{4\pi\|\mathbf{r}\|_2} \boldsymbol{\theta} \cos\theta H_0$$
$$\times \iint \exp(-2jk\mathbf{M} \cdot \mathbf{r}')dS' \quad (5)$$

where $\mathbf{M} = \hat{\mathbf{r}} - \left(\hat{\mathbf{r}} \cdot \hat{\mathbf{n}}\right)\hat{\mathbf{n}}$

Reference [30] introduced a method that converts the double integral into a summation form as follows.

The detailed derivations from Eq.(6) to Eq.(9) are given in Appendix A.

$$\mathbf{E_s}(\mathbf{r}) = \sum_{n=1}^{N} \mathbf{A_n T_n} \tag{6}$$

$$\begin{cases} \mathbf{A_n} = -j\eta \dfrac{\exp(jk\|\mathbf{r}\|_2)}{4\pi\|\mathbf{r}\|_2}\cos\theta H_0 \dfrac{\mathbf{M^*}\cdot\mathbf{a_n}}{2k\|\mathbf{M}\|_2^2}\mathbf{M}\cdot\Delta\mathbf{a_n}\boldsymbol{\theta} \\ \mathbf{T_n} = \exp(-2jk\mathbf{M}\cdot\mathbf{a_{n+1}}) - \exp(-2jk\mathbf{M}\cdot\mathbf{a_n}) \\ \mathbf{M}\cdot\Delta\mathbf{a_n} \neq 0 \end{cases} \tag{7}$$

where $\mathbf{r}' = [x_1, x_2]$, $\mathbf{M} = [m_1, m_2]$ are Euclidean coordinates in the polygon plate, $\mathbf{M^*} = [m_2, -m_1]$ is the vector obtained by rotating $\mathbf{M}$ through $90°$ and $\mathbf{a_1}\ldots\mathbf{a_N}$ are vertices of the polygon plate. Set $\mathbf{a_{N+1}} = \mathbf{a_1}$ and $\Delta\mathbf{a_n} = \mathbf{a_{n+1}} - \mathbf{a_n}$ $(1 \leq n \leq N)$.

$$\begin{cases} \mathbf{A_n} = -\eta\dfrac{\exp(jk\|\mathbf{r}\|_2)}{4\pi\|\mathbf{r}\|_2}\cos\theta H_0 \dfrac{\mathbf{M^*}\cdot\Delta\mathbf{a_n}}{\|\mathbf{M}\|_2^2} \\ \qquad\quad \times \sin c\,(k\mathbf{M}\cdot\Delta\mathbf{a_n})\,\boldsymbol{\theta} \\ \mathbf{T_n} = \exp\left(-2jk\mathbf{M}\cdot\dfrac{\mathbf{a_n}+\mathbf{a_{n+1}}}{2}\right) \\ \\ \mathbf{M}\cdot\Delta\mathbf{a_n} = 0 \end{cases} \tag{8}$$

When $\mathbf{M} = [0,0]$, Eq.(5) can be rewritten as

$$\mathbf{E_s}(\mathbf{r}) \cong -2j\eta k\frac{\exp(jk\|\mathbf{r}\|_2)}{4\pi\|\mathbf{r}\|_2}\cos\theta H_0 A\boldsymbol{\theta} \tag{9}$$

where A is the area of the polygon plate.

The location of the scattering center is determined by the phase of $\mathbf{E_s}(\mathbf{r})$. Consequently, the information of scattering center position is involved in $\mathbf{T_n}$. According to the geometry relationship between $\mathbf{M}$ and $\mathbf{a_n}$, the locations of the scattering centers are analyzed as follows.

1. $\mathbf{M}\cdot\triangle\mathbf{a_n} \neq 0$

Eq.(7) indicates the scattering centers are vertices of polygon plate. The position remains invariant with the change of aspect angles. This type of scattering center is known as LSC. It can be observed within a wide range of aspect angles.

2. $\mathbf{M}\cdot\mathbf{a_n} = 0$

Eq.(8) indicates the scattering centers are the midpoints of the polygon plate edges. This type of scattering center is known as DSC. DSC can be observed only within narrow elevation and/or azimuth angles.

Suppose the polygon plate resides in the **XOY** plane as shown in Fig. 1, the unit normal vector $\mathbf{n} = [0, 0, 1]$ and $\mathbf{r} = [\sin\theta\cos\varphi, \sin\theta\sin\varphi, \cos\theta]$.

$$\mathbf{M}\cdot\Delta\mathbf{a_n} = L_n\sin\theta\sin(\varphi - \bar\varphi_n) \tag{10}$$

where L_n is the length of the nth side of polygon plate and $\bar\varphi_n$ is the azimuth angle of $\hat{\mathbf{r}}$ when $\hat{\mathbf{r}}\cdot\Delta\mathbf{a_n} = 0$.

The underlined equation **E2** in Eq.(A4) can be rewritten as Eq.(11) when $\mathbf{M}\cdot\Delta\mathbf{a_n} = 0$.

$$\mathbf{E2} = \underline{\sin c\,[kL_n\sin\theta\sin(\varphi - \bar\varphi_n)]}$$
$$\cdot e^{-2jk(x_m\sin\theta\cos\varphi + y_m\sin\theta\sin\varphi)} \tag{11}$$

where $[x_m, y_m]$ are the coordinates of midpoints of polygon plate sides.

According to the ASC model presented in [31], $L_n\sin\theta$ is the length and $\bar\varphi_n$ is the orientation angle of DSC.

3. $\mathbf{M} = [0, 0]$ (i.e. the electromagnetic wave illuminates the polygon plate vertically)

The scattering center can be equivalent to the origin point $(0, 0)$.

B. SAR IMAGES OF THE TYPICAL POLYGON PLATE

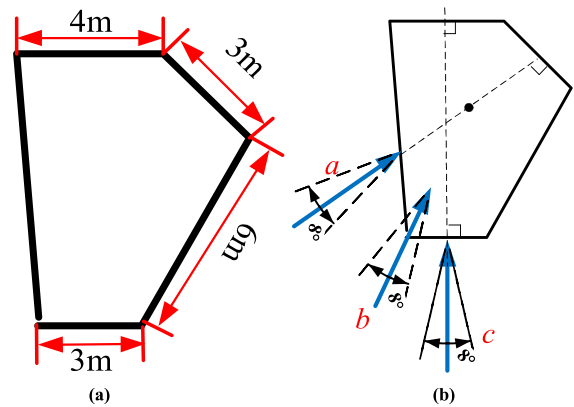A typical polygon plate is applied in the SAR simulation and listed in Fig. 2.

FIGURE 2. A typical polygon plate (a) the size of the typical polygon plate(b) the geometric relationship between the vector M and polygon plates.

The size of the typical polygon plate is shown in Fig. 2(a). The geometric relationship between the vector $\mathbf{M}$ and the polygon plate are shown in Fig. 2(b). Fig. 3 depicts SAR images of the typical polygon plate under various azimuth angle ranges. Pitch angles of SAR simulation remain $30°$. The range and azimuth resolutions are 0.1m. Fig. 3(d) is the SAR image where $\hat{\mathbf{i}} = [0, 0, -1]$.

Fig. 3 verifies the mathematical analysis in the previous section. The vertices and midpoints of polygon plate edges correspond to LSCs and DSCs respectively. LSCs of polygon plates can be observed under wide azimuth angles. Conversely, the DSCs only can be observed when the incident wave direction satisfies $\mathbf{M}\cdot\mathbf{a_n} = 0$. Eq.(11) indicates that the length of DSCs is $\sin\theta$ times the length of the polygon plate sides as shown in Fig.3(a) and Fig.3(c). Since the length of DSCs is always related to the real size of the single-curved surfaces or edges of targets and observation angles, DSCs are the key features to recognize targets and reconstruct their structure.

III. CSCs OF TYPICAL DIHEDRAL CORNERS

Typical dihedral corners are composed of two rectangular plates. Therefore, the single-bouncing mechanism of dihedral corners can be understood from section II. The effect of multiple reflections produces novel characteristics. The single-bouncing mechanism can be described by LSCs or DSCs while the multi-bouncing scattering
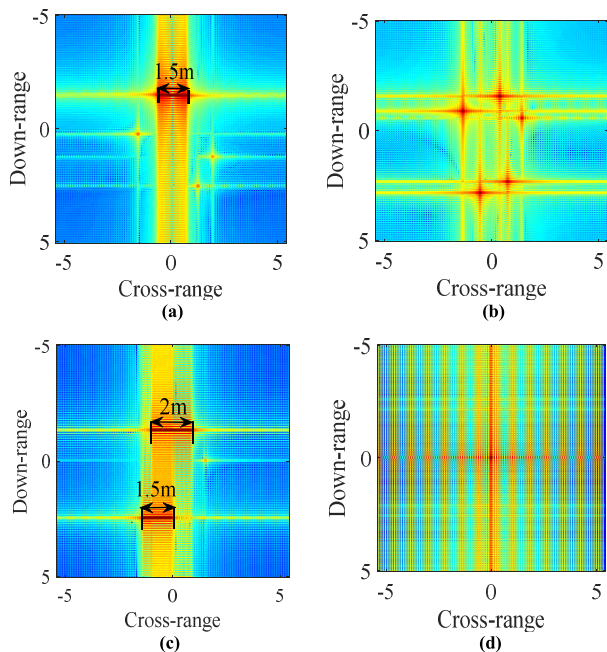
FIGURE 3. The SAR images of the typical polygon plate under different aspect angle.

characteristics cannot be described by the listed three types of scattering centers accurately. Hence, CSCs are proposed as the supplements of three typical kinds of scattering centers. CSCs widely exist in coupling structures such as dihedral, trihedral etc. They will become strong scattering centers under some specific conditions. CSCs are referred to as unstable scattering centers, the location of which varies with the changes of aspect angles.

Because the incident wave direction is usually different from the reflected wave direction in multi-bouncing scattering, the locations of CSCs are not the direct projection of scattering centers onto the line of sight (LOS). Fortunately, the multi-bouncing scattering mechanism is similar to the bistatic scattering mechanism, so the monostatic-and-bistatic equivalence theorem (MBET) is applied to analyze CSCs.

According to MBET: If the scattering centers can be observed in the bistatic mode, they can be equivalent to the scattering centers in monostatic mode. As shown in Fig.4, the equivalent monostatic radar is located at the bistatic angle bisector $\hat{\mathbf{r}}_{\mathbf{B}} = \left(\hat{\mathbf{r}}_{\mathbf{T}} + \hat{\mathbf{r}}_{\mathbf{R}} \right) / 2$. $-\hat{\mathbf{r}}_{\mathbf{T}}$ and $\hat{\mathbf{r}}_{\mathbf{R}}$ denote the transmitting and receiving directions respectively.

MBET has been widely applied to analyze the characteristics of bistatic scattering centers. Reference [32] presented that the scattering centers induced by edge diffraction are located at the intersections of the cone-shaped target bottom and the plane constructed by the z-axis and the bistatic angle bisector $\hat{\mathbf{r}}_{\mathbf{B}}$. Reference [13] used a monostatic scattering center to equate the scattering center induced by creeping wave in bistatic mode. Reference [33] investigated the sliding scattering center induced by the reflected wave in bistatic mode by tracing the equivalent propagation path along the direction of $\hat{\mathbf{r}}_{\mathbf{B}}$.
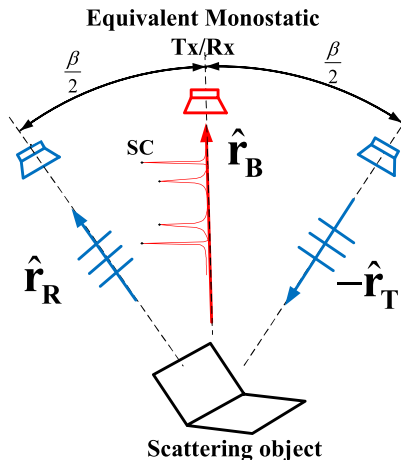

FIGURE 4. The equivalent relationship between bistatic and monostatic radar.

According to the work listed above, it is reasonable to utilize MBET to analyze the characteristics of bistatic scattering centers. Due to the similarity between the bistatic scattering mechanism and the multi-bouncing scattering mechanism, MBET can also be applied to investigate the multi-bouncing scattering.

A. ORTHOGONAL DIHEDRAL CORNER

Orthogonal dihedral corners exist in many SAR scenes, such as trunk and ground, ship and ocean surface. The orthogonal dihedral corners are strong scattering targets and they can be observed within a wide range of observation orientation. The reason is that the CSC is a strong scattering center within a wide range of observation orientation.
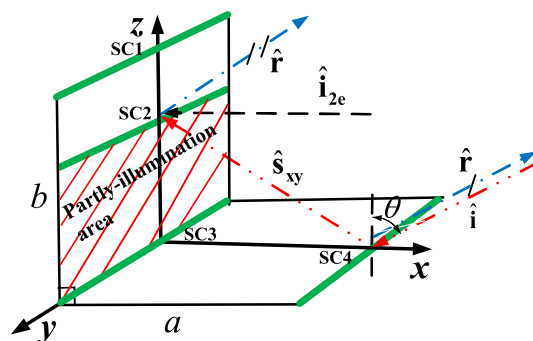

FIGURE 5. Scattering geometry of orthogonal dihedral corners.

The incident ($\hat{\mathbf{i}}$), received ($\hat{\mathbf{r}}$), reflected by plate ($\hat{\mathbf{s}}_{\mathbf{xy}}$) wave direction and the incident direction of equivalent monostatic $\mathbf{i}_{\mathbf{2e}}$ are shown in Fig. 5. when $\varphi_i = 0°$, $\mathbf{i}_{\mathbf{2e}}$ is written as Eq.(12) in the monostatic mode, which is deduced in Appendix B.

$$\mathbf{i}_{\mathbf{2e}} = -2\hat{\mathbf{x}} \sin \theta_i \qquad (12)$$

Eq.(12) indicates that the incident direction of equivalent monostatic $\mathbf{i}_{\mathbf{2e}}$ is vertical to the plate of orthogonal dihedral corner residing in the *yoz* plane.

The locations of single-bouncing scattering centers in HRRPs are the direct projection of scattering centers onto LOS. The locations of single-bouncing scattering centers in HRRPs are

$$\begin{cases} y_{LSC1} = 0 \\ y_{LSC2} = a\sin\theta_i \\ y_{LSC3} = b\cos\theta_i \end{cases} \qquad (13)$$

where y_{LSC1}, y_{LSC2} and y_{LSC3} denote the down-range of three scattering centers illustrated as SC3, SC4, SC1 in Fig.5.

Since the incident direction of equivalent monostatic is vertical to the plate 2 of the orthogonal dihedral corner, the double reflection produces a very strong echo within a wide range of observation orientation. Eq.(9) has demonstrated that the CSCs will be compressed in the original point because the incident direction of equivalent monostatic about double reflection is vertical to the plate of the dihedral corner.
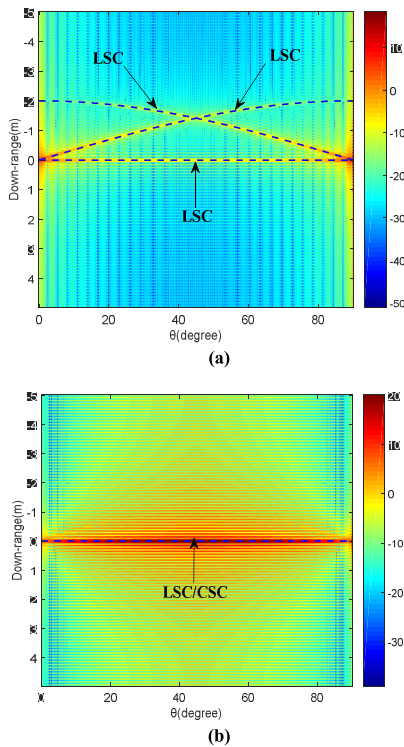

(a)

(b)

FIGURE 6. (a) partial HRRPs of orthogonal dihedral corners (b) full HRRPs of orthogonal dihedral corners.

Fig. 6 shows the HRRPs of orthogonal dihedral corners with $a = 2\text{m}$ and $b = 2\text{m}$, where Fig.6(a) is the HRRPs when only considering single-bouncing scattering and Fig.6(b) is the HRRPs when considering both the single-bouncing and double-bounce scattering. The HRRP is obtained by the Inverse Fourier Transform (IFT) of wideband backscattered fields which are computed by shooting and bouncing rays (SBR) based on CST. The carrier frequency is 10GHz and the bandwidth is 1.5GHz with a step of 15MHz. The elevation angle θ of LOS changes from 0° to 90° and

the azimuth angle of LOS remains $\varphi = 0°$. The single-bouncing scattering characteristics of dihedral corners can be understood from scattering characteristics of polygon plates. Therefore, the single-bouncing scattering centers of dihedral corners are three points when the incident directions of rays are set as shown in Fig. 5. The dash lines in Fig. 6(a) are the theoretical locations of three scattering centers and they are consistent with the peak values of HRRPs. As shown in Fig. 6(b), the double-bounce scattering is the dominant element of the scattering field and the single-bounce scattering centers are overwhelmed. The scattering centers generated by double-bounce scattering are referred to as CSCs. In this case, LSCs of orthogonal dihedral corners cannot be observed in the HRRPs. However, LSCs can be observed in SAR images as shown in Section IV, because the azimuth dimension accumulation is considered.

B. OBTUSE DIHEDRAL CORNER

In contrast to the orthogonal dihedral corners, Eq. (12) indicates that the incident direction of equivalent monostatic $\mathbf{i}_{2e}$ is not vertical to the plate of obtuse dihedral corners which is illuminated by double-bouncing rays. As a result, the CSC of the obtuse dihedral corner is not the strong scattering center and the obtuse dihedral corners are difficult to be detected in a monostatic case. Furthermore, the CSC of obtuse dihedral corners is not compressed in the original point, because the incident direction of equivalent monostatic is not vertical to the plate of dihedral corners.
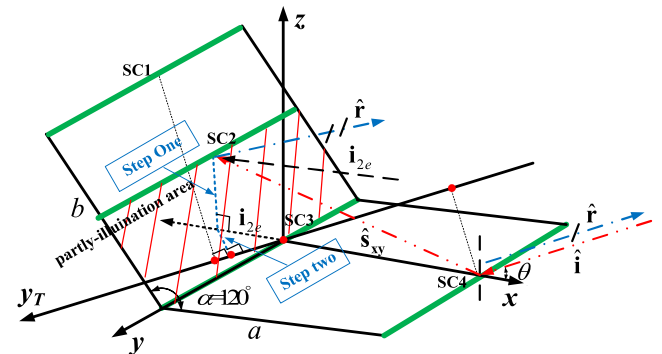

FIGURE 7. Scattering geometry of obtuse dihedral corners.

As shown in Fig. 7, the illumination area related to the double-bouncing is sometimes not equal to the plate of dihedral corners, which depends on the pitch angle of the incident wave. The method for calculating the equivalent length of plate 2 is introduced in [34].

As shown in Fig. 8, the observation aspects can be divided into three conditions as follows.

$$\begin{cases} 0 \leq \theta_i \leq \gamma_n & \text{partly-illumination} \\ \gamma_n \leq \theta_i \leq \pi - (n-1)\alpha & \text{full-illumination} \\ \pi - (n-1)\alpha \leq \theta_i \leq \alpha & \text{non-illumination} \end{cases} \qquad (14)$$

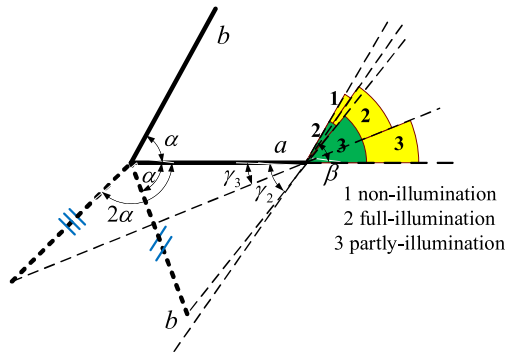where n is the bouncing times and α is the opening angles of dihedral corners.

FIGURE 8. Geometry for calculating the equivalent length of plates.

Based on the geometry in Fig. 8, the equivalent length of the plate is

$$
\widetilde{L}_n \begin{cases} \dfrac{a \sin \theta}{\sin [\alpha (n-1) + \theta]}, & 0 \le \theta_i \le \gamma_n \\ b & \gamma_n \le \theta_i \le \pi - (n-1)\alpha \\ 0 & \pi - (n-1)\alpha \le \theta_i \le \alpha \end{cases} \quad (15)
$$

If the azimuth angle of the incident wave is set as $\varphi_i = 0°$, the vector $\mathbf{i_{2e}}$ will satisfy

$$
\mathbf{i_{2e}} \cdot \Delta a_\mathbf{n} = 0 \quad (16)
$$

where $\mathbf{i_{2e}}$ is the vector of the incident direction of equivalent monostatic observation and $\Delta a_\mathbf{n}$ is the vector of the nth edge of the obtuse dihedral corner.
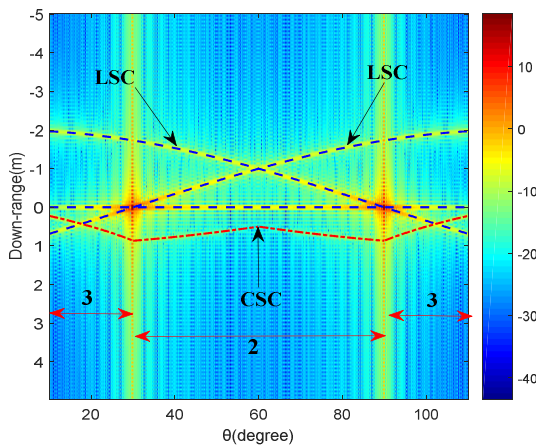

FIGURE 9. HRRPs of the 120° obtuse dihedral corner.

As introduced in section II, the midpoints of edges $\{\Delta a_\mathbf{n}\}$ labeled as green lines in Fig. 7 contribute the scattering centers. Fig. 9 demonstrates that the locations of scattering centers corresponding to single-bouncing scattering in the HRRPs (illustrated as blue dash lines) are the direct projection of scattering centers onto the LOS. However, the locations of scattering centers related to double-bouncing should be determined by two steps as shown in Fig. 7. Firstly, determine the projection of scattering centers onto the equivalent monostatic observation orientation $\mathbf{i_{2e}}$, and then project the previous projection onto the first incident LOS $\hat{\mathbf{i}}$. The location
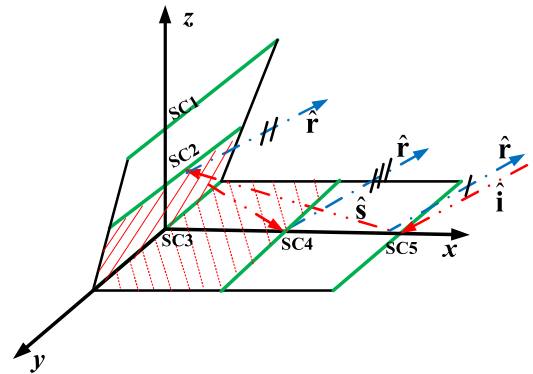
FIGURE 10. Scattering geometry of acute dihedral corners.

of the CSC in HRRP can be expressed as

$$
\begin{cases} y_{\mathrm{csc}} = b \cos (\pi - \alpha) \cos \theta, & 0 \le \theta \le \dfrac{\pi}{6} \\ y_{\mathrm{csc}} = \dfrac{a \sin \theta}{\sin (\alpha + \theta)} \cos (\pi - \alpha) \cos \theta, & \dfrac{\pi}{6} \le \theta \le \dfrac{\pi}{3} \end{cases} \quad (17)
$$

Fig. 9 shows the HRRP sequences of the 120° obtuse dihedral corner with $a = 2$m and $b = 2$m. The parameters are set as follows. The carrier frequency is 10GHz and the bandwidth is 1.5GHz with a step of 15MHz. The elevation angle θ of LOS changes from 10° to 110° and the azimuth angle of LOS remains $\varphi = 0°$. The theoretical location of CSC is illustrated by the red dash line in the Fig. 9. As shown in Fig. 9, the theoretical locations of four scattering centers are consistent with the peak values of HRRPs. The number 2 and 3 represent the ranges of elevation angles of full-illumination and partly-illumination respectively. In addition, when the elevation angles are 30° and 90°, the incident wave illuminates the plate of obtuse dihedral corner vertically; Thus, the sidelobes are visible at the two elevation angles in Fig. 9.

C. ACUTE DIHEDRAL CORNER

One of the differences among acute dihedral corners and orthogonal/obtuse dihedral corners is the ray bouncing times. The ray bouncing times in acute dihedral corner is always more than two times which result in difficult analysis.

The CSCs corresponding to multiple-bouncing scattering are determined by applying the trick that the specular reflection is regarded as a straight light propagation in the mirror domain. This trick has been proposed in [34]. The sketch of propagation in the mirror domain is shown in Fig. 11.

According to the geometry, the angles in Fig. 11 can be obtained as follows.

$$
\begin{cases} \angle 1 = \arccos \left[\dfrac{\mathbf{l_{n2}} \cdot \left(-\hat{\mathbf{i}}\right)}{|\mathbf{l_{n2}}|} \right] = (n-1)\alpha + \theta, \\ \quad n = 2k, \ k \in N^+ \\ \angle 2 = \arccos \left[\dfrac{\mathbf{l_{n1}} \cdot \left(-\hat{\mathbf{i}}\right)}{|\mathbf{l_{n1}}|} \right] = (n-1)\alpha + \theta, \\ \quad n = 2k - 1, \ k \in N^+ \\ \alpha = \arccos \left[\dfrac{\mathbf{l_1} \cdot \mathbf{l_2}}{|\mathbf{l_1}| |\mathbf{l_2}|} \right] \end{cases} \quad (18)
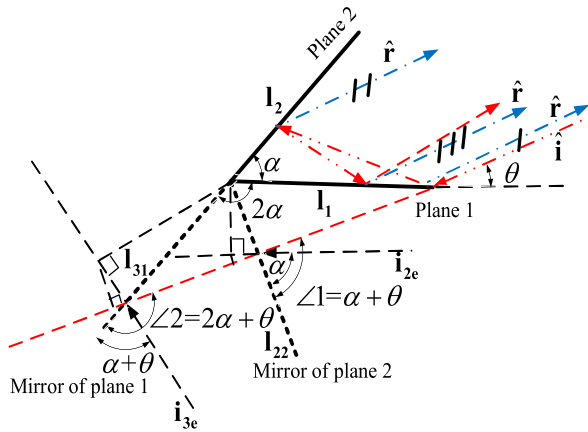$$

FIGURE 11. View of multiple bouncing about acute dihedral corners.

FIGURE 12. HRRPs of 60° acute dihedral corner.

where $\mathbf{l_{n1}}$, $\mathbf{l_{n2}}$ represent the mirror of $\mathbf{l_1}$, $\mathbf{l_2}$ respectively and n is the number of reflections.

The incident direction of equivalent monostatic observation $\mathbf{i_{ne}}$ is

$$\begin{cases} \arccos\left[\dfrac{(-\mathbf{i_{ne}}) \cdot \mathbf{l_{n2}}}{|\mathbf{l_{n2}}|}\right] = \dfrac{n}{2}\alpha & n = 2k, \ k \in N^+ \\[3mm] \arccos\left[\dfrac{(-\mathbf{i_{ne}}) \cdot \mathbf{l_{n1}}}{|\mathbf{l_{n1}}|}\right] = \dfrac{n-1}{2}\alpha + \theta & n = 2k-1, \ k \in N^+ \end{cases}$$

(19)

After two projection operation as shown in Fig.11, the positions of CSCs of the acute dihedral corner in the HRRP are deduced based on Eq.(18) and Eq.(19).

$$y_{\mathrm{csc}\,n} = \begin{cases} -\widetilde{L}_n \cos\left(\dfrac{n}{2}\alpha\right) \underline{\cos\left(\dfrac{n-2}{2}\alpha + \theta\right)}, \\[2mm] \qquad\qquad n = 2k, \ k \in N^+ \\[3mm] -\widetilde{L}_n \cos\left(\dfrac{n-1}{2}\alpha + \theta\right) \underline{\cos\left(\dfrac{n-1}{2}\alpha\right)}, \\[2mm] \qquad\qquad n = 2k-1, \ k \in N^+ \end{cases}$$

(20)

The underlined factors in Eq.(20) are actually scaled factor $K(t) = \cos(\theta(t)/2)$, $\theta(t)$ is the bistatic angle [35].

The equivalent length of plates $\widetilde{L}_n$ for acute dihedral corners are calculated by Eq.(15).

The 60° acute dihedral corner is chosen to verify the above analysis. For the 60° dihedral corner, the positions of CSCs in the HRRP are

$$\begin{cases} y_{\mathrm{csc}\,2} = -\dfrac{1}{2}\widetilde{L}_2 \cos\theta \\[3mm] y_{\mathrm{csc}\,3} = -\dfrac{1}{2}\widetilde{L}_3 \cos\left(\dfrac{\pi}{3} + \theta\right) \end{cases}$$

(21)

where

$$\widetilde{L}_2 = \dfrac{|\mathbf{l_1}| \sin\theta}{\sin\left(\dfrac{2\pi}{3} - \theta\right)}, \quad \widetilde{L}_3 = \begin{cases} |\mathbf{l_1}| & \dfrac{\pi}{6} \leq \theta \leq \dfrac{\pi}{3} \\[3mm] \dfrac{|\mathbf{l_1}| \sin\theta}{\sin\left(\dfrac{\pi}{3} - \theta\right)} & 0 \leq \theta \leq \dfrac{\pi}{6} \end{cases}$$
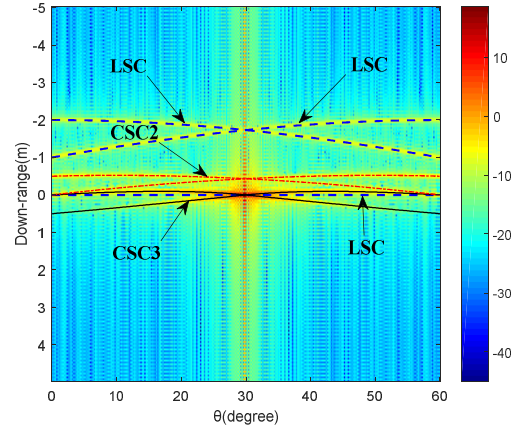
(22)

Fig. 12 shows the HRRPs of the 60° acute dihedral corner with $a = 2\mathrm{m}$ and $b = 2\mathrm{m}$. The parameters are set as follows. The carrier frequency is 10GHz and the bandwidth is 1.5 GHz with a step of 15MHz. The elevation angle θ of LOS changes from 0° to 60° and the azimuth angle of LOS remains 0°. As shown in Fig. 12, the dash lines are the theoretical locations of seven scattering centers and they are consistent with the peak values of HRRPs. Especially, two pairs of CSCs are well located in the HRRPs as CSC2 and CSC3.

The sidelobes are visible at 30° elevation angle and the phenomenon can be explained by Eq.(19). When the elevation angle is 30°, Eq.(19) is rewritten as

$$\arccos\left[\dfrac{(-\mathbf{i_{3e}}) \cdot \mathbf{l_{31}}}{|\mathbf{l_{31}}|}\right] = \dfrac{\pi}{3} + \dfrac{\pi}{6} = \dfrac{\pi}{2}$$

(23)

Eq.(23) indicates that the $\mathbf{i_{3e}}$ is vertical to the plate 1 of acute dihedral corners; Thus, the CSC3 will be compressed in the origin point and the third bouncing scattering contributes more to the 60° dihedral corners scattering.

As shown in Fig. 12, the CSCs' number of the acute dihedral corners is larger than orthogonal/obtuse dihedral corners. The reason is the opening angle of acute dihedral corners is smaller than orthogonal and obtuse dihedral corners. Therefore, the coupling scattering characteristics of acute dihedral corners are more complicated. To investigate the principle of multi-bouncing scattering in acute dihedral corners, the relationship between bouncing times and opening angle is analyzed as follows.

Due to the symmetric structure, only the rays are reflected from one of the plates are traced. The elevation angle of incident wave changes from 0° to α. where α is the opening angle of the dihedral corner.

According to the mirror projection of the propagation path as shown in Fig.11, the bouncing times n can be calculated by

$$(n-1)\alpha \leq \pi - \theta_i \leq n\alpha$$

(24)

Hence, n should satisfy

$$n = \left[\frac{\pi - \theta_i}{\alpha}\right] \qquad (25)$$

where $[\cdot]$ stands for rounding the element to the nearest integer greater than or equal to that element. Thus, the maximum bouncing times is $n = [\pi/\alpha]$ and the minimum bouncing times is $n = [\pi/\alpha - 1]$.
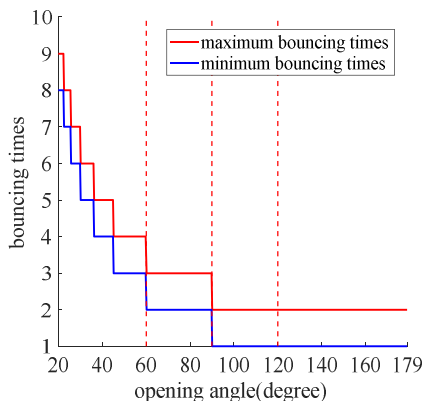

FIGURE 13. The relationship between opening angle and bouncing times.

Fig. 13 depicts the maximum bouncing times and minimum bouncing times of dihedral corners with different opening angles. The red dash lines mark the three types dihedral corner simulated in this paper.

Fig. 14 depicts the relationship between the elevation angle of the incident wave and bouncing times according to Eq. (25). The red and blue lines correspond to the bouncing times of rays which illuminate plate 1 and plate 2 at first bounce respectively. As shown in Fig. 14, the lines are symmetric with respect to $\theta_i = \alpha/2$ due to the symmetric structure of dihedral corner. According to the foregoing analysis, the number of CSCs m (except the CSCs located at origin point) is equal to

$$m(\theta) = [n_1(\theta) - 1] + [n_2(\theta) - 1] \qquad (26)$$

where $n_1(\theta)$ and $n_2(\theta)$ are the bouncing times of two plates and θ is the elevation angle.

According to Eq.(26): When $\alpha = 120°$, $m \equiv 1$. It can be verified by Fig.9. When $\alpha = 60°$, $m \equiv 4$ except at $\theta_i = 30°$. It can be verified by Fig.12.

It should be noted that when the incident direction of equivalent monostatic $\mathbf{i}_{ne}$ is vertical to one of the plates of the dihedral corner, Eq. (26) is not suitable to obtain m, such as $\theta_i = 30°$ in Fig. 9 and $\alpha = 90°$. Because the CSCs are located at the origin point under this condition. Fortunately, this circumstance takes place at specific elevation angles which can be calculated by Eq.(19).

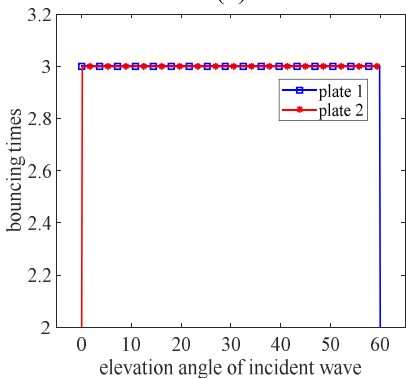## IV. THE SAR IMAGING SIMULATIONS OF TYPICAL DIHEDRAL CORNERS VIA EM COMPUTATION

In this section, the SAR simulations of dihedral corners are conducted. The scattering field is computed by SBR. The SAR imaging technology applied in this section is simple
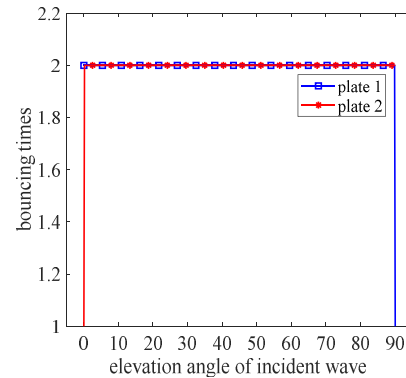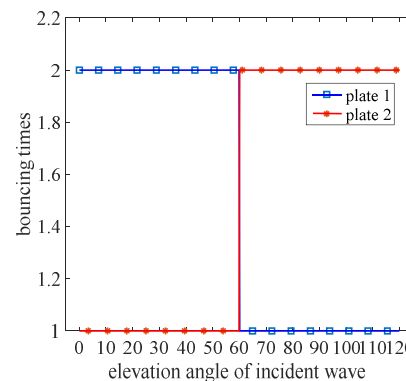
FIGURE 14. The relationship between elevation angle of the incident wave and bouncing times. (a) 90° dihedral corner (b) 120° obtuse dihedral corner (c) 60° acute dihedral corner.

spotlight SAR imaging, and the translational motion is properly compensated; only the rotation between the sensor and the target is considered. The imaging process involves two steps: 2-D interpolation and 2-D IFFT. More details can be referred to [36]. The geometry of SAR simulation is shown in Fig. 15 and the parameters of imaging are set as TABLE 1. The parameters of the three types of dihedral corners are the same as those in Section III.

A. ORTHOGONAL DIHEDRAL CORNER
Fig. 16 shows the SAR images of an orthogonal dihedral corner. If only the single-bouncing scattering is taken into consideration, the scattering centers are midpoints of
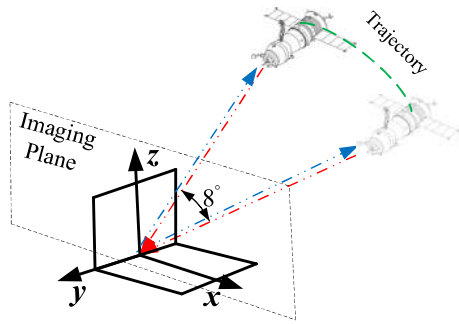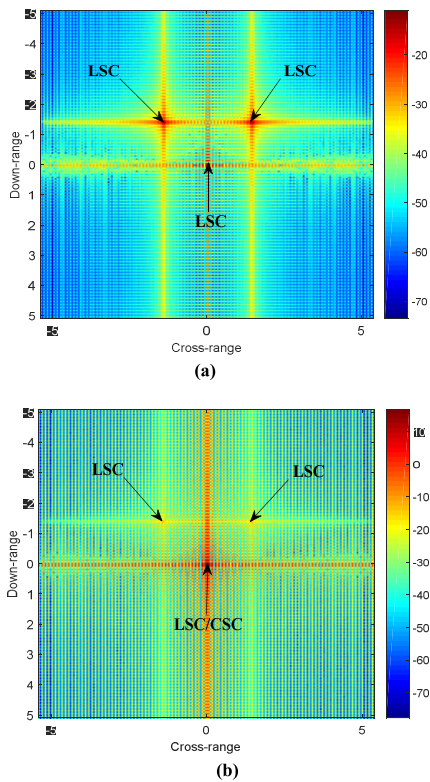
FIGURE 15. The geometry of SAR imaging simulation.

(a)

(b)

FIGURE 16. The SAR images of orthogonal dihedral corners $\theta_i \in [41°, 49°]$ (a) only single-bouncing scattering is considered (b) both the single-bouncing and double-bouncing scattering are considered.

TABLE 1. Parameters of SAR simulation.

Carrier frequency	10GHz
Bandwidth	1.5GHz
Frequency stepping interval	15MHz
Total aspect angle variation	8°
Angle interval	0.08°
Down-range resolution	0.1m
Cross-range- resolution	0.1m

three edges of dihedral corners. The scattering centers are obvious in the SAR images because the energies of scattering centers are nearly equal as shown in Fig.16(a). However,
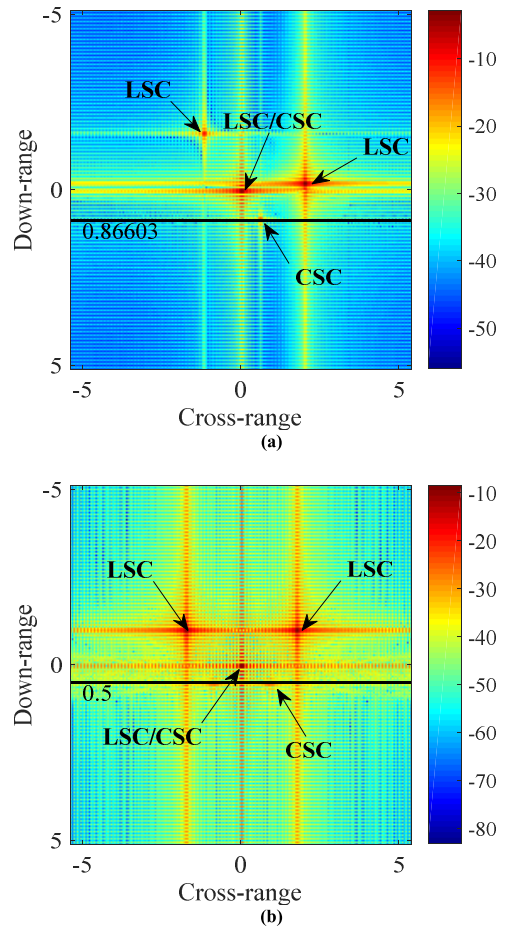

(a)

(b)

FIGURE 17. The SAR images of 120° dihedral corners (a) $\theta_i \in [26°, 34°]$ (b) $\theta_i \in [50°, 58°]$.

when the double-bouncing scattering is considered, the scattering centers corresponding to single-bouncing scattering are so weak that they are hardly observed in the SAR images because the CSCs related to double-bouncing scattering are strong scattering centers and other types of scattering centers are overwhelmed by CSCs in the SAR images. Compared with the scattering centers in HRRPs analyzed in section III part A, the scattering centers corresponding to single-bouncing scattering are more obvious due to azimuth dimension accumulation.

B. OBTUSE DIHEDRAL CORNER

Fig. 17 shows the SAR images of an 120° obtuse dihedral corner with different pitch angles. There is only one CSC in the dihedral corner as analysis in section III part B, because only one plate of the dihedral corner can be illuminated by double-bouncing rays for each time. What's more, the CSC of the obtuse dihedral corner is more obvious than the orthogonal dihedral corner because the CSC is not compressed in the origin point, and the scattering intensity is the almost same.

To make the validation of theoretical derivation more convincing, the range locations of CSCs are calculated
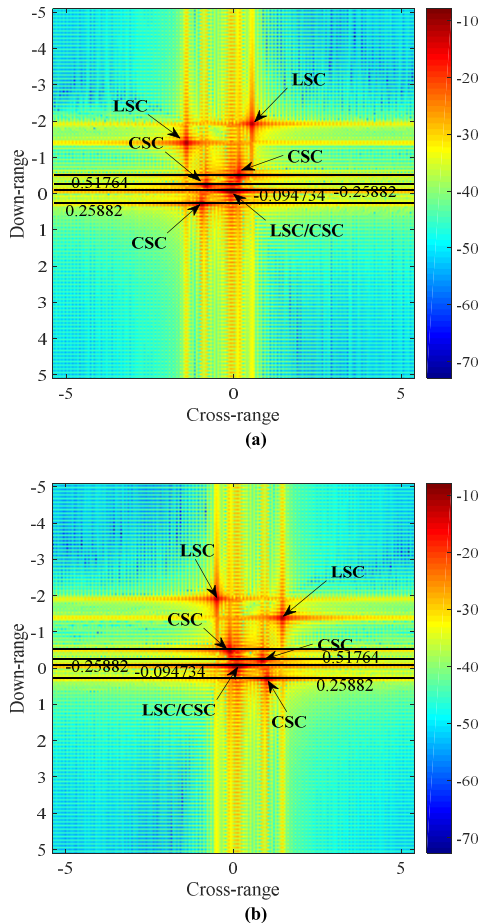
FIGURE 18. The SAR images of acute dihedral corners (a) $\theta_i \in [41°, 49°]$ (b) $\theta_i \in [71°, 79°]$.

according to Eq. (20) and labeled as black solid lines. As shown in Fig.17 and Fig.18, the CSCs are all located at the solid lines, which verify the correctness of theoretical derivation once more.

C. ACUTE DIHEDRAL CORNER

Fig.18 shows the SAR images of an acute dihedral corner with different pitch angles. The CSCs of acute dihedral corners can be observed obviously in the SAR images and they may cause confusion for target recognition. However, the CSCs also reflect target features and they can be used for feature extraction. The number of CSCs of acute dihedral corners is more than orthogonal and obtuse dihedral corners, because the bouncing times of acute dihedral corners are more than other types dihedral corners.

The SAR images and HRRPs of three types of dihedral corners indicate that the CSCs are the key features to distinguish different types of dihedral corners. CSC is the strong scattering center of the orthogonal dihedral corner and located at the origin point, which does not change with LOS. The location of the CSC of obtuse dihedral corner varies with the LOS. A continuous line and an isolated point

corresponding to the CSC can be detected in the HRRPs and SAR images respectively. The number of CSCs of acute dihedral corners is always more than 2, which is the obvious feature in the HRRPs and SAR images. Therefore, the three types of dihedral corners can be well distinguished based on the coupling scattering characteristics of dihedral corners.

V. CONCLUSION

Dihedral corners are typical coupling structures which are also abstract models of many complex coupling structures. The dihedral corners can be replaced by several scattering centers corresponding to single-bouncing and multi-bouncing scattering mechanism respectively. In this paper, the two types of scattering centers are analyzed in detail.

The scattering characteristics of polygon plates are investigated at first. According to the theoretical derivation, the locations of scattering centers are deduced. Based on polygon plate scattering understanding, the CSCs are proposed to investigate the multi-bouncing scattering characteristics. MBET is utilized to obtain the positions of CSCs in the HRRPs, and these theoretical analyses coincide well with the EM simulation data. Moreover, the relationship between the number of CSCs and opening angles are presented, which conducts much in analyzing the multi-bouncing scattering of dihedral corners. Finally, the CSCs of three types of dihedral corners are analyzed accurately in SAR images.

Coupling scattering analysis is a hot but difficult topic in radar imaging, feature extraction, etc. As for the coupling scattering characteristics of dihedral corners, they have not been investigated clearly. There are still some questions that should be further investigated. Firstly, to simplify the analysis, only the pitch angle variation is considered in this paper. In the actual SAR scene, the azimuth angles may also change. Secondly, the roughness of the dihedral corner plates could impact the coupling scattering. The hypothesis that the plates are perfectly smooth and conducting deviates the actual structures.

The several questions will be further investigated in the near future. Furthermore, the parametric model of CSCs will be presented. The model-based algorithm of ATR that considers the coupling scattering will be studied.

APPENDIX A

Let $\mathbf{M} = [m_1, m_2]$ be a constant vector in the plane of $\mathbf{S}$ and $[x_1, x_2]$ are the Euclidean coordinates of $\mathbf{r}'$.

$$\iint \exp(-2jk\mathbf{M} \cdot \mathbf{r}')dS'$$
$$= \frac{1}{2jk \|\mathbf{M}\|_2^2} \int_{\partial S} \exp(-2jk\mathbf{M} \cdot \mathbf{r}') (m_2 dx_1 - m_1 dx_2) \quad \text{(A1)}$$

Proof: Apply the stokes' theorem to the right side of Eq.(A1):

$$
\int_{\partial S} \exp(-2jk\mathbf{M}\cdot\mathbf{r}')\,(m_2 dx_1 - m_1 dx_2)
$$

$$
= \iint_{S} \left\{ \begin{array}{l} -m_1 \dfrac{\partial\left[\exp\left(-2jk\mathbf{M}\cdot\mathbf{r}'\right)\right]}{\partial x_1} \\[2mm] -m_2 \dfrac{\partial\left[\exp\left(-2jk\mathbf{M}\cdot\mathbf{r}'\right)\right]}{\partial x_2} \end{array} \right\} dx_1 dx_2
$$

$$
= \iint_{S} 2jk\left(m_1^2 + m_2^2\right)\exp\left(-2jk\mathbf{M}\cdot\mathbf{r}'\right) dx_1 dx_2
$$

$$
= 2jk\,\|\mathbf{M}\|_2^2 \iint_{S} \exp\left(-2jk\mathbf{M}\cdot\mathbf{r}'\right) dx_1 dx_2
$$

To obtain Eq.(6)-(9), apply the Eq.(A1) to the integral of Eq.(5), then Eq.(5) is rewritten as:

$$
\mathbf{E_s}\,(\mathbf{r}) \cong -\frac{\exp(jk\,\|\mathbf{r}\|_2)}{4\pi\,\|\mathbf{r}\|_2}\frac{\cos\theta H_0 \eta}{\|\mathbf{M}\|_2^2}\boldsymbol{\theta}
$$
$$
\cdot \int_{\partial S} \exp(-2jk\mathbf{M}\cdot\mathbf{r}')\,(m_2 dx_1 - m_1 dx_2) \quad \text{(A2)}
$$

$$
\mathbf{E_s}\,(\mathbf{r}) \cong -\frac{\exp(jk\,\|\mathbf{r}\|_2)}{4\pi\,\|\mathbf{r}\|_2}\frac{\cos\theta H_0 \eta}{\|\mathbf{M}\|_2^2}\boldsymbol{\theta}\,(J_1 + \cdots + J_N) \quad \text{(A3)}
$$

Let $\mathbf{M}^* = [m_2, -m_1]$ is the vector obtained by rotating $\mathbf{M}$ through an angle of 90°, $\mathbf{a_1}\ldots\mathbf{a_N}$ are vertices of polygon plate and $\mathbf{r}'(t) = (1-t)\mathbf{a_n} + t\mathbf{a_{n+1}}\ t\in[0,1]$ is the parametric representation of the nth side of polygon plate. Set $\mathbf{a_{N+1}} = \mathbf{a_1}$ and for $1 \le n \le N$ set $\Delta\mathbf{a_n} = \mathbf{a_{n+1}} - \mathbf{a_n}$.

$$
J_n = \int_{\partial S_n} \exp(-2jk\mathbf{M}\cdot\mathbf{r}')\,(m_2 dx_1 - m_1 dx_2)
$$

$$
= \int_0^1 \left(\mathbf{M}^* \cdot \Delta\mathbf{a_n}\right)\exp\{-2jk\mathbf{M}\cdot[(1-t)\mathbf{a_n} + t\mathbf{a_{n+1}}]\}\,dt
$$

$$
= \left(\mathbf{M}^* \cdot \Delta\mathbf{a_n}\right)e^{-2jk\mathbf{M}\cdot\mathbf{a_n}}\frac{e^{-2jk\mathbf{M}\cdot\Delta\mathbf{a_n}} - 1}{-2jk\mathbf{M}\cdot\Delta\mathbf{a_n}}
$$

$$
= \frac{\left(\mathbf{M}^* \cdot \Delta\mathbf{a_n}\right)}{-2jk\mathbf{M}\cdot\Delta\mathbf{a_n}}\left(e^{-2jk\mathbf{M}\cdot\mathbf{a_{n+1}}} - e^{-2jk\mathbf{M}\cdot\mathbf{a_n}}\right) \rightarrow \mathbf{E1}
$$

$$
= \left(\mathbf{M}^* \cdot \Delta\mathbf{a_n}\right)e^{-2jk\mathbf{M}\cdot\frac{\mathbf{a_n}+\mathbf{a_{n+1}}}{2}}\frac{\sin\left(k\mathbf{M}\cdot\Delta\mathbf{a_n}\right)}{k\mathbf{M}\cdot\Delta\mathbf{a_n}}
$$

$$
= \underline{\left(\mathbf{M}^* \cdot \Delta\mathbf{a_n}\right)\sin c\,(k\mathbf{M}\cdot\Delta\mathbf{a_n})\,e^{-2jk\mathbf{M}\cdot\frac{\mathbf{a_n}+\mathbf{a_{n+1}}}{2}}} \rightarrow \mathbf{E2} \quad \text{(A4)}
$$

The positions of scattering centers are determined by the phase of $\mathbf{E_s}\,(\mathbf{r})$. Consequently, the scattering centers of polygon plates are the vertices according to **E1** underlined in the Eq.(A4) or the midpoints of the edges according to **E2**. However, the scattering center intensity decreases rapidly when $\mathbf{E_s}\,(\mathbf{r})$ is expressed in **E2** form and $\mathbf{M}\cdot\Delta\mathbf{a_n} \ne 0$. Therefore, the positions of scattering centers should be discussed according to $\mathbf{M}\cdot\Delta\mathbf{a_n}$.

when $\mathbf{M}\cdot\Delta\mathbf{a_n} \ne 0$, **E1** is applied to express $\mathbf{E_s}\,(\mathbf{r})$ as

$$
\begin{cases}
\mathbf{E_s}\,(\mathbf{r}) = \displaystyle\sum_{n=1}^{N} \mathbf{A_n T_n} \\[3mm]
\mathbf{A_n} = -j\eta\dfrac{\exp(jk\,\|\mathbf{r}\|_2)}{4\pi\,\|\mathbf{r}\|_2}\cos\theta H_0 \dfrac{\mathbf{M}^* \cdot \mathbf{a_n}}{2k\,\|\mathbf{M}\|_2^2\,\mathbf{M}\cdot\Delta\mathbf{a_n}}\boldsymbol{\theta} \\[3mm]
\mathbf{T_n} = \exp(-2jk\mathbf{M}\cdot\mathbf{a_{n+1}}) - \exp(-2jk\mathbf{M}\cdot\mathbf{a_n})
\end{cases}
$$
$$\text{(A5)}$$

when $\mathbf{M}\cdot\Delta\mathbf{a_n} = 0$, the $\mathbf{E_s}\,(\mathbf{r})$ is rewritten as:

$$
\begin{cases}
\mathbf{E_s}\,(\mathbf{r}) = \displaystyle\sum_{n=1}^{N} \mathbf{A_n T_n} \\[3mm]
\mathbf{A_n} = -\eta\dfrac{\exp(jk\,\|\mathbf{r}\|_2)}{4\pi\,\|\mathbf{r}\|_2}\cos\theta H_0 \dfrac{\mathbf{M}^* \cdot \Delta\mathbf{a_n}}{\|\mathbf{M}\|_2^2} \\[3mm]
\qquad \times \sin c\,(k\mathbf{M}\cdot\Delta\mathbf{a_n})\,\boldsymbol{\theta} \\[3mm]
\mathbf{T_n} = \exp\left(-2jk\mathbf{M}\cdot\dfrac{\mathbf{a_n}+\mathbf{a_{n+1}}}{2}\right)
\end{cases} \quad \text{(A6)}
$$

when $\mathbf{M} = [0,0]$, the Eq.(5) can be simplified directly as

$$
\mathbf{E_s}\,(\mathbf{r}) \cong -2j\eta k\frac{\exp(jk\,\|\mathbf{r}\|_2)}{4\pi\,\|\mathbf{r}\|_2}\cos\theta H_0 A\boldsymbol{\theta} \quad \text{(A7)}
$$

where A is area of the polygon plate.

APPENDIX B

$$
\begin{cases}
\hat{\mathbf{i}} = -(\hat{\mathbf{x}}\sin\theta_i\cos\varphi_i + \hat{\mathbf{y}}\sin\theta_i\sin\varphi_i + \hat{\mathbf{z}}\cos\theta_i) \\
\hat{\mathbf{r}} = \hat{\mathbf{x}}\sin\theta_r\cos\varphi_r + \hat{\mathbf{y}}\sin\theta_r\sin\varphi_r + \hat{\mathbf{z}}\cos\theta_r \\
\hat{\mathbf{s}}_{\mathbf{xy}} = -\hat{\mathbf{x}}\sin\theta_i\cos\varphi_i - \hat{\mathbf{y}}\sin\theta_i\sin\varphi_i + \hat{\mathbf{z}}\cos\theta_i
\end{cases} \quad \text{(B1)}
$$

where, θ and φ are the pitch and azimuth angles in the sphere coordinate system respectively.

In the monostatic mode, Eq. (B1) can be rewritten as

$$
\begin{cases}
\hat{\mathbf{i}} = -(\hat{\mathbf{x}}\sin\theta_i\cos\varphi_i + \hat{\mathbf{y}}\sin\theta_i\sin\varphi_i + \hat{\mathbf{z}}\cos\theta_i) \\
\hat{\mathbf{r}} = \hat{\mathbf{x}}\sin\theta_i\cos\varphi_i + \hat{\mathbf{y}}\sin\theta_i\sin\varphi_i + \hat{\mathbf{z}}\cos\theta_i \\
\hat{\mathbf{s}}_{\mathbf{xy}} = -\hat{\mathbf{x}}\sin\theta_i\cos\varphi_i - \hat{\mathbf{y}}\sin\theta_i\sin\varphi_i + \hat{\mathbf{z}}\cos\theta_i
\end{cases} \quad \text{(B2)}
$$

If the azimuth of the incident wave is set as $\varphi_i = 0°$ (i.e. the incident wave direction is set as shown in Fig. 5), and Eq. (B2) can be simplified as

$$
\hat{\mathbf{i}} = -(\hat{\mathbf{x}}\sin\theta_i + \hat{\mathbf{z}}\cos\theta_i)
$$
$$
\hat{\mathbf{r}} = \hat{\mathbf{x}}\sin\theta_i + \hat{\mathbf{z}}\cos\theta_i
$$
$$
\hat{\mathbf{s}}_{\mathbf{xy}} = -\hat{\mathbf{x}}\sin\theta_i + \hat{\mathbf{z}}\cos\theta_i \quad \text{(B3)}
$$

It is easy to prove that

$$
\mathbf{i_{2e}} = \hat{\mathbf{s}}_{\mathbf{xy}} - \hat{\mathbf{r}} \quad \text{(B4)}
$$

From Eq.(B4), the $\mathbf{i_{2e}}$ can be written in Cartesian coordinates as

$$
\mathbf{i_{2e}} = -2\hat{\mathbf{x}}\sin\theta_i \quad \text{(B5)}
$$

REFERENCES

[1] M. Xing, X. Jiang, R. Wu, F. Zhou, and Z. Bao, "Motion compensation for UAV SAR based on raw radar data," *IEEE Trans. Geosci. Remote Sens.*, vol. 47, no. 8, pp. 2870–2883, Aug. 2009.

[2] G. Sun, M. Xing, X. Xia, Y. Wu, and Z. Bao, "Robust ground moving-target imaging using deramp–keystone processing," *IEEE Trans. Geosci. Remote Sens.*, vol. 51, no. 2, pp. 966–982, Feb. 2013.

[3] F. Zhou, R. Wu, M. Xing, and Z. Bao, "Approach for single channel SAR ground moving target imaging and motion parameter estimation," *IET Radar, Sonar Navigat.*, vol. 1, no. 1, pp. 59–66, Feb. 2007.

[4] M. Liu, S. Chen, J. Wu, F. Lu, X. Wang, and M. Xing, "SAR target configuration recognition via two-stage sparse structure representation," *IEEE Trans. Geosci. Remote Sens.*, vol. 56, no. 4, pp. 2220–2232, Apr. 2018.

[5] G. Dong, G. Kuang, N. Wang, and W. Wang, "Classification via sparse representation of steerable wavelet frames on Grassmann manifold: Application to target recognition in SAR image," *IEEE Trans. Image Process.*, vol. 26, no. 6, pp. 2892–2904, Jun. 2017.

[6] J. Pei, Y. Huang, W. Huo, J. Wu, J. Yang, and H. Yang, "SAR imagery feature extraction using 2DPCA-based two-dimensional neighborhood virtual points discriminant embedding," *IEEE J. Sel. Topics Appl. Earth Observ. Remote Sens.*, vol. 9, no. 6, pp. 2206–2214, Jun. 2016.

[7] S. Ohno, S. Kidera, and T. Kirimoto, "Efficient SOM-based ATR method for SAR imagery with azimuth angular variations," *IEEE Geosci. Remote Sens. Lett.*, vol. 11, no. 11, pp. 1901–1905, Nov. 2014.

[8] M. Amoon and G.-A. Rezai-rad, "Automatic target recognition of synthetic aperture radar (SAR) images based on optimal selection of Zernike moments features," *Comput. Vis., IET*, vol. 8, no. 2, pp. 77–85, Apr. 2014.

[9] Y. He, S.-Y. He, Y.-H. Zhang, G.-J. Wen, D.-F. Yu, and G.-Q. Zhu, "A forward approach to establish parametric scattering center models for known complex radar targets applied to SAR ATR," *IEEE Trans. Antennas Propag.*, vol. 62, no. 12, pp. 6192–6205, Dec. 2014.

[10] Y. Cong, B. Chen, H. Liu, and B. Jiu, "Nonparametric Bayesian attributed scattering center extraction for synthetic aperture radar targets," *IEEE Trans. Signal Process.*, vol. 64, no. 18, pp. 4723–4736, Sep. 2016.

[11] J. Duan, L. Zhang, M. Xing, Y. F. Wu, and M. Wu, "Polarimetric target decomposition based on attributed scattering center model for synthetic aperture radar targets," *IEEE Geosci. Remote Sens. Lett.*, vol. 11, no. 12, pp. 2095–2099, Dec. 2014.

[12] B. Ding, G. Wen, X. Huang, C. Ma, and X. Yang, "Target recognition in synthetic aperture radar images via matching of attributed scattering centers," *IEEE J. Sel. Topics Earth Observ. Remote Sens.*, vol. 10, no. 7, pp. 3334–3347, Jul. 2017.

[13] Q.-Y. Qu, K.-Y. Guo, and X.-Q. Sheng, "An accurate bistatic scattering center model for extended cone-shaped targets," *IEEE Trans. Antennas Propag.*, vol. 62, no. 10, pp. 5209–5218, Oct. 2014.

[14] K.-Y. Guo, Q.-F. Li, X.-Q. Sheng, and M. Gashinova, "Sliding scattering center model for extended streamlined targets," *Prog. Electromagn. Res.*, vol. 139, pp. 499–516, Aug. 2013.

[15] C. Beaudoin, T. Horgan, G. Demartinis, M. J. Coulombe, A. J. Gatesman, and W. E. Nixon, "Fully polarimetric bistatic radar calibration with modified dihedral objects," *IEEE Trans. Antennas Propag.*, vol. 66, no. 2, pp. 937–950, Feb. 2018.

[16] C. M. H. Unal, R. J. Niemeijer, J. S. van Sinttruyen, and L. P. Ligthart, "Calibration of a polarimetric radar using a rotatable dihedral corner reflector," *IEEE Trans. Geosci. Remote Sens.*, vol. 32, no. 4, pp. 837–845, Jul. 1994.

[17] T.-J. Chen, T.-H. Chu, and F.-C. Chen, "A new calibration algorithm of wide-band polarimetric measurement system," *IEEE Trans. Antennas Propag.*, vol. 39, no. 8, pp. 1188–1192, Aug. 1991.

[18] H. Hirosawa and Y. Matsuzaka, "Calibration of a cross-polarized SAR image using dihedral corner reflectors," *IEEE Trans. Geosci. Remote Sens.*, vol. 26, no. 5, pp. 697–700, Sep. 1988.

[19] G. Smith and L. M. H. Ulander, "A model relating VHF-band backscatter to stem volume of coniferous boreal forest," *IEEE Trans. Geosci. Remote Sens.*, vol. 38, no. 2, pp. 728–740, Mar. 2000.

[20] J. A. Marble and A. O. Hero, "See through the wall detection and classification of scattering primitives," *Proc. SPIE, Radar Sensor Technol. X*, vol. 6210, May 2006.

[21] J. A. Jackson, "Analytic physical optics solution for bistatic, 3D scattering from a dihedral corner reflector," *IEEE Trans. Antennas Propag.*, vol. 60, no. 3, pp. 1486–1495, Mar. 2012.

[22] T. Griesser and C. A. Balanis, "Backscatter analysis of dihedral corner reflectors using physical optics and the physical theory of diffraction," *IEEE Trans. Antennas Propag.*, vol. 35, no. 10, pp. 1137–1147, Oct. 1987.

[23] T. Griesser and C. A. Balanis, "Dihedral corner reflector backscatter using higher order reflections and diffractions," *IEEE Trans. Antennas Propag.*, vol. AP-35, no. 11, pp. 1235–1247, Nov. 1987.

[24] A. Michaeli, "A closed form physical theory of diffraction solution for electromagnetic scattering by strips and 90° dihedrals," *Radio Sci.*, vol. 19, no. 2, pp. 609–616, Mar./Apr. 1984.

[25] K.-Y. Guo, Q.-Y. Qu, and X.-Q. Sheng, "Geometry reconstruction based on attributes of scattering centers by using time-frequency representations," *IEEE Trans. Antennas Propag.*, vol. 64, no. 2, pp. 708–720, Feb. 2016.

[26] Y. Jin, J. M. F. Moura, and N. O'Donoughue, "Experimental study of extended target imaging by time reversal SAR," in *Proc. IEEE Int. Conf. Acoust., Speech Signal Process.*, Taipei, Taiwan, Apr. 2009, pp. 2109–2112.

[27] I. de Arriba-Ruiz, F. Pérez-Martínez, and J. M. Muñoz-Ferreras, "Time-reversal-based multipath mitigation technique for ISAR images," *IEEE Trans. Geosci. Remote Sens.*, vol. 51, no. 5, pp. 3119–3138, May 2013.

[28] I. de Arriba-Ruiz, J. M. Muñoz-Ferreras, and F. Pérez-Martínez, "Multipath mitigation techniques based on time reversal concept and superresolution algorithms for inverse synthetic aperture radar imaging," *IET Radar, Sonar Navigat.*, vol. 7, no. 4, pp. 413–421, Apr. 2013.

[29] J. M. F. Moura and Y. Jin, "Detection by time reversal: Single antenna," *IEEE Trans. Signal Process.*, vol. 55, no. 1, pp. 187–201, Jan. 2007.

[30] W. B. Gordon, "Far-field approximations to the Kirchoff-Helmholtz representations of scattered fields," *IEEE Trans. Antennas Propag.*, vol. 23, no. 4, pp. 590–592, Jul. 1975.

[31] M. J. Gerry, L. C. Potter, I. J. Gupta, and A. V. D. Merwe, "A parametric model for synthetic aperture radar measurements," *IEEE Trans. Antennas Propag.*, vol. 47, no. 7, pp. 1179–1188, Jul. 1999.

[32] X. Ai, X. Zou, Y. Li, J. Yang, and S. Xiao, "Bistatic scattering centres of cone-shaped targets and target length estimation," *Sci. China Inf. Sci.*, vol. 55, no. 12, pp. 2888–2898, 2012.

[33] Q. Y. Qu, K. Y. Guo, and X. Q. Sheng, "Scattering centers induced by creeping waves on streamlined cone-shaped targets in bistatic mode," *IEEE Antennas Wireless Propag. Lett.*, vol. 14, pp. 462–465, 2015.

[34] D. Ao, Y. Li, C. Hu, and W. Tian, "Accurate analysis of target characteristic in bistatic SAR images: A dihedral corner reflectors case," *Sensors*, vol. 18, no. 1, p. 24, Dec. 2017.

[35] M. Martorella, J. Palmer, J. Homer, B. Littleton, and I. D. Longstaff, "On bistatic inverse synthetic aperture radar," *IEEE Trans. Aerosp. Electron. Syst.*, vol. 43, no. 3, pp. 1125–1134, Jul. 2007.

[36] J. L. Walker, "Range-Doppler imaging of rotating objects," *IEEE Trans. Aerosp. Electron. Syst.*, vol. ANE-16, no. 1, pp. 23–52, Jan. 1980.

ZHIMING XU was born in Shandong, China, in 1995. He received the B.S. degree in electronic engineering from Wuhan University, Wuhan, China, in 2017. He is currently pursuing the Ph.D. degree with the State Key Laboratory of Complex Electromagnetic Environmental Effects on Electronics and Information System, National University of Defense Technology, Changsha, China.

His research interests include radar imaging and radar target recognition.

XIAOFENG AI was born in Sichuan, China, in 1983. He received the B.S. and M.S. degrees in electronic engineering and the Ph.D. degree in information and communication engineering from the National University of Defense Technology (NUDT), Changsha, China, in 2005, 2007, and 2013, respectively.

He is currently a Lecturer with NUDT. His research interests include radar imaging and feature extraction.

QIHUA WU was born in Jiangsu, China, in 1990. He received the B.S. degree in communication engineering from Nanjing University, Nanjing, China, in 2013, and the M.S. degree in information and communication engineering from the National University of Defense Technology, Changsha, China, in 2015, where he is currently pursuing the Ph.D. degree at the CEMEE.

His research interests include radar imaging techniques and radar signal processing.

FENG ZHAO was born in Jiangsu, China, in 1978. He received the B.S. degree in electronic engineering and the Ph.D. degree in information and communication engineering from the National University of Defense Technology (NUDT), Changsha, China, in 2001 and 2007, respectively.

He is currently an Associate Professor with NUDT. His research interests include radar system design and detection techniques of tracking and guiding radar.

SHUNPING XIAO was born in Jiangxi, China, in 1964. He received the B.S. and Ph.D. degrees in electronic engineering from the National University of Defense Technology (NUDT), Changsha, China, in 1986 and 1995, respectively.

He is currently a Professor with NUDT. His research interests include radar target recognition and radar signal processing. He is a Senior Member of CIE.

• • •